Univerzita Karlova v Praze
Matematicko-fyzikální fakulta

BAKALÁŘSKÁ PRÁCE

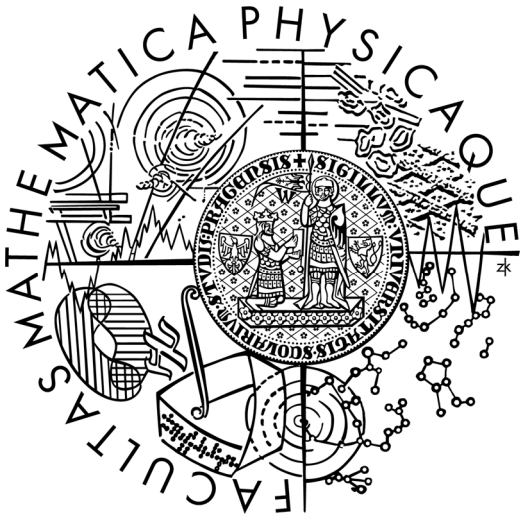

Ivan Ivani

Studium relaxorových ferroelektrik pomocí Ramanova rozptylu

Katedra fyziky kondenzovaných látek

Vedoucí bakalářské práce: *Ing. Jiří Hlinka, PhD., Fyzikální ústav AV ČR*

Studijní program: *Fyzika, Fyzika kondenzovaných soustav a materiálů*

2008

I would like to thank my supervisor Jiří Hlinka for allowing me to write my bachelor's report in Academy of Science, for many answers on relaxors and Raman spectroscopy, for patience shown explaining those things to me, for providing me with right articles and especially for directing me in the right direction during my work. It would have been much harder without him. Also I would like to thank Ivan Gregora for his explanations of the Raman microscope, for his patience while showing me how to work on micro-Raman spectrometer and mainly for his contribution in explaining the problems that occurred during our measurement. I should not forget Jan Pokorný for his article about Raman spectroscopie and time spent waiting for me to finish my measurment. I should not forget Sophie Marika Reed for her kind advises about my report.

Prohlašují, že jsem svou bakalářskou práci napsal samostatně a výhradně s použitím citovaných pramenů. Souhlasím se zapůjčováním práce.

V Praze dne Ivan Ivani

Název práce: *Studium relaxorových ferroelektrik pomocí Ramanova rozptylu*
Autor: *Ivan Ivani*
Katedra (ústav): *Katedra fyziky kondenzovaných látek*
Vedoucí bakalářské práce: *Ing. Jiří Hlinka, PhD., Fyzikální ústav AV ČR, Na Slovance 2, Praha 8*
e-mail vedoucího: *hlinka@fzu.cz*

Abstrakt: *Komplexní perovskity relaxorového typu, t.j. materiály se strukturou odvozenou substitucemi iontů Ti v mřížce prototypického ferroelektrika $PbTiO_3$, jsou známy svými vynikajícími dielektrickými a piezoelektrickými vlastnostmi. Původ relaxorového chování i velikost piezoodezvy je předmětem intezivního výzkumu. Naším úkolem bylo přispět k vysvětlení jejich vlastností pomoci studia dynamiky krystalové mřížky pomocí Ramanove spektroskopie. Toto jsme provedli srovnávaním studií spekter polarizovaného Ramanova rozptylu v systému $Pb(Mg_{1/3}Nb_{2/3})O_3$ - $PbTiO_3$ a analyzováním spektrálných přispěvků.*
Klíčová slova: *relaxory, ferroelektrika, Ramanova spektroskopie*

Title: *Relaxor ferroelectrics by Raman scattering*
Author: *Ivan Ivani*
Department: *Department of Condensed Matter Physics*
Supervisor: *Ing. Jiří Hlinka, PhD., Institute of Physics Acad. of Scien. CZ, Na Slovance 2, Prague 8*
Supervisor's e-mail address: *hlinka@fzu.cz*

Abstract: *Complex perovskites of relaxor type, i.e. mainly materials with crystal structure derived from that of $PbTiO_3$ by mixed substitutions at Ti position, are known for their remarkable dielectric and piezoelectric properties. The $Pb(Mg_{1/3}Nb_{2/3})O_3$ is perhaps the simplest of the strong ABO_3 relaxors, but its physics has been and remains challenging despite extensive research. Questions about the origin of their relaxor behaviour as well as of the extraordinary piezoelectric properties belongs to most challenging themes in the current ferroelectric material research. The $Pb(Mg_{1/3}Nb_{2/3})\ O_3$ - $PbTiO_3$ single crystals properly orientated exhibit the extremely large values of the dielectric constant, ultrahigh strain, giant piezoeffect and electrostriction. This is related to the fact that the crystal domains easily orient during poling so that the maximum response is obtained. Subject of this work is to contribute to such aim by performing a comparative polarized Raman scattering study of crystals of $Pb(Mg_{1/3}Nb_{2/3})TiO_3$ - $PbTiO_3$ system.*
Keywords: *relaxors, ferroelectrics, Raman scattering, Raman spectroscopy*

Introduction

Complex perovskites of relaxor type, i.e. mainly materials with crystal structure derived from that of $PbTiO_3$ by mixed substitutions at Ti position, are known for their remarkable dielectric and piezoelectric properties. The $Pb(Mg_{1/3}Nb_{2/3})O_3$ is perhaps the simplest of the strong ABO_3 relaxors, but its physics has been and remains challenging despite extensive research. Questions about the origin of their relaxor behavior as well as of the extraordinary piezoelectric properties belong to most challenging themes in the current ferroelectric material research. The $Pb(Mg_{1/3}Nb_{2/3})\ O_3$ - $PbTiO_3$ single crystals properly orientated exhibit the extremely large values of the dielectric constant, ultrahigh strain, giant piezoeffect and electrostriction. This is related to the fact that the crystal domains easily orient during poling so that the maximum response is obtained. Subject of this work is to contribute to the study of relaxor ferroelectrics by investigating lattice dynamics, performing a comparative polarized Raman scattering study of crystals of $Pb(Mg_{1/3}Nb_{2/3})\ O_3$ - $PbTiO_3$ system.

This report is organized as follows. First chapter gives a brief introduction to the Raman scattering, both within the framework of classical and quantum theory. Also, in this part, the Micro-Raman instrumentation for performing Raman scattering investigation is described. In second chapter we consider relaxor ferroelectrics, their characteristics and differences from normal ferroelectrics, as well as their applications. Chapter three is reserved for our measurements. Here the work that has been made is demonstrated. We began by describing the work that has been made on $PbTiO_3$ sample, measured in two different incident light direction geometries. Then measurement of the PMN30%PT system is presented. In the last chapter we discuss problems that occurred during measurements, compare the two systems and our work is briefly concluded.

Chapter 1

Raman Spectroscopy – Basic Theory, Experimental Techniques, Instrumentation

1.1 Introduction

In 1928 Sir Chandrasekhra Venkata Raman discovered the phenomenon that bears his name. Raman scattering or the Raman effect is an inelastic scattering of photons by collective excitations (phonons, plasmons, magnons) or single-particle (electrons, electron-hole pairs). Raman scattering gives important information about the properties of such type of excitations in molecules or a condensed matter objects. Raman scattering is usually investigated in the range of $10^4 – 10^2$ cm^{-1}.

1.2 Basic Theory of Raman scattering

1.2.1 The Classical Theory

The scattered light can be conveniently divided in two parts: a strong, elastic scattering, called *Rayleigh scattering*, which has the same frequency as the incident beam and the other, inelastic part, called *Raman scattering,* is very weak and has frequency $\nu_0 - \nu_m$, so called *Stokes*, or $\nu_0 + \nu_m$, called *anti-Stokes,* where ν_m is a vibrational frequency of a molecule or solid.

The classic theory of Raman scattering is based on the idea that the electromagnetic field of the incident light induces, in the system, a time dependent dipole moment

$$\boldsymbol{M}(t) = \sum e_i \boldsymbol{r_i}(t) \tag{1.1}$$

The electric field of the electromagnetic wave (laser beam) is given by

$$\boldsymbol{E} = E_0 \cos 2\pi\nu_0 t \tag{1.2}$$

where the E_0 is the vibrational amplitude and ν_0 is the frequency of the laser. Since ν_0 is much larger than the vibrational frequencies of the atoms, only the electrons but not the atoms can respond to the light field $\boldsymbol{E}$. By irradiating the molecule an electric dipole moment $\boldsymbol{P}$ is induced:

$$\boldsymbol{P} = \alpha \boldsymbol{E} \tag{1.3}$$

where α is the electronic polarizability. If the molecule is vibrating with a frequency ν_m the nuclear displacement q is written

$$q = q_0 \cos 2\pi\nu_m t \tag{1.4}$$

where q_0 is the vibrational amplitude. For small amplitude of vibration, α is a linear function of q. Thus, we can write

$$\alpha = \alpha_0 + \left(\frac{\partial \alpha}{\partial q}\right)_0 q_0 + \frac{1}{2}\left(\frac{\partial^2 \alpha}{\partial q^2}\right)_0 q_0^2 + \ldots \tag{1.5}$$

where α_0 is the polarizability at the equilibrium position. The *first-order Raman effect* is determined by the linear term in *q*, *the second-order Raman effect* by quadratic term in *q,* etc.

Combining Eq. 1.5 with Eq. 1.2, 1.3 and 1.4 we obtain

$$P = \alpha_0 E_0 \cos 2\pi\upsilon_0 t + \frac{1}{2}\left(\frac{\partial \alpha}{\partial q}\right)_0 q_0 E_0 \left[\cos\left\{2\pi\left(\upsilon_0 + \upsilon_m\right)t\right\} + \cos\left\{2\pi\left(\upsilon_0 - \upsilon_m\right)t\right\}\right] \tag{1.6}$$

The first term describes elastic or *Rayleigh scattering*, while the second term corresponds to the Raman scattering of frequency $\nu_0 + \nu_m$ (*anti-Stokes*) and $\nu_0 - \nu_m$ (*Stokes*). If $\left(\frac{\partial \alpha}{\partial q}\right)_0$ is zero, the vibration is not Raman active.

In general, the direction of the induced dipole moment $\boldsymbol{P}$ doesn't coincide with the direction of electric field $\boldsymbol{E}$. The relation (1.3) is a vectorial relation and thus the polarizability is a second-order tensor. We can write the Eq. 1.3 in matrix form as

$$\begin{bmatrix} P_x \\ P_y \\ P_z \end{bmatrix} = \begin{bmatrix} \alpha_{xx} & \alpha_{xy} & \alpha_{xz} \\ \alpha_{yx} & \alpha_{yy} & \alpha_{yz} \\ \alpha_{zx} & \alpha_{zy} & \alpha_{zz} \end{bmatrix} \begin{bmatrix} E_x \\ E_y \\ E_z \end{bmatrix} \tag{1.7}$$

The first matrix on the right-hand of (1.7) is called the *polarizability tensor*. Consequently, the derivatives $\left(\frac{\partial \alpha}{\partial q}\right)_0$ should be also considered as tensorial quantities.

If this tensor is symmetric $\alpha_{xy} = \alpha_{yx}$, $\alpha_{xz} = \alpha_{zx}$, $\alpha_{zy} = \alpha_{yz}$, there always exists a coordinate system in which the polarizability tensor is a diagonal matrix [1]. Such axes are called *principle axis of polarizability*.

1.2.2 The Quantum Mechanical Theory

In terms of the corpuscular theory of light Rayleigh scattering corresponds to an *elastic collision* between photon and crystal, whereas Raman scattering corresponds to *inelastic collision* in which the photon either loses one (first-order scattering) or more (higher-order scattering) quanta of vibrational energy (Stokes lines) or acquires one or more quanta (anti-Stokes lines). By making a downward or upward transition between two discrete energy states, the system emits or absorbs radiation, as shown on Figure 1.1.

Figure 1.1 immediately accounts for the higher intensity of the Stokes lines compared to the anti-Stokes lines, because the population of the ground vibrational

level is much greater and therefore the chance for incident photon to find the system in an excited vibrational level is much smaller. According to Bose-Einstein statistics, the ratio between the two is temperature dependent and proportional to $\exp(\hbar\Omega / k_B T)$. Therefore by recording both Stokes and anti-Stokes lines we can obtain the temperature inside the scattering volume.

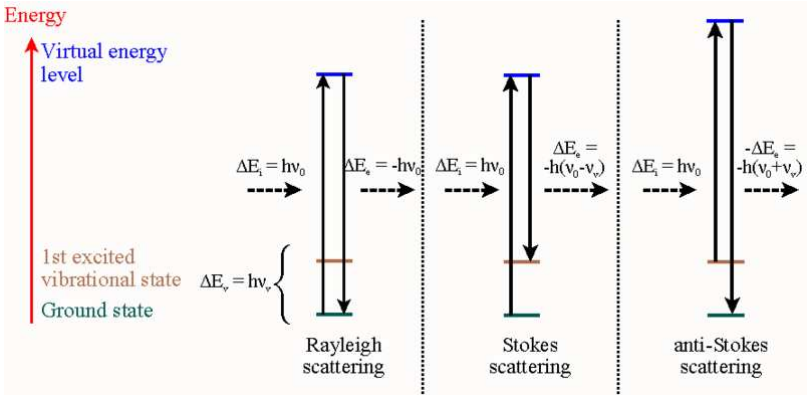

Figure 1.1 Energy level diagram for Rayleigh scattering, Stokes scattering and anti-Stokes scattering [15].

The probability to observe a scattered particle in a given quantum state per solid angle unit per frequency unit or the *spectral differential cross section,* can be expressed by

$$\frac{d^2\sigma}{d\Omega d\omega_S} \propto \omega_S^4 \sum_j \left| e_{S\rho} R_{\rho\lambda}^{(j)}(\vec{k}, \omega_I, -\omega) e_{I\lambda} \right|^2 \left\langle q_j(\vec{k}) q_j^*(\vec{k}) \right\rangle_\omega \tag{1.8}$$

where $\mathbf{e}_\mathrm{I}$, $\mathbf{e}_\mathrm{S}$ are unit polarization vectors of the incident and scattered light [Figure 1.2], ***k*** is a quasi-momentum and $R_{\rho\lambda}$ is the Raman tensor. This tensor is called Raman tensor and is defined as

$$R_{\rho\lambda}^{(j)} = \left(\frac{\partial \alpha_{\rho\lambda}(\omega_I)}{\partial q_j^*} \right)_0 \tag{1.9}$$

The Raman tensor governs a relation between the incoming and outgoing electric fields for a vibrational mode *j*. Raman scattering is possible only if the corresponding element of the Raman tensor is non-zero and the possibility for the element of Raman tensor to be non-zero is limited by crystal lattice point symmetry.

1.2.3 Selection Rules

Group theory allows one to determine the symmetry species of the vibrational modes and also which elements of the Raman tensor are non-zero. Raman tensors are tabulated in many books on Raman scattering (e.g. [2]).

The Porto notation is a useful convention for representing experimental scattering geometries. The notation stands for $\mathbf{k}_I$ ($\mathbf{e}_I$, $\mathbf{e}_S$) $\mathbf{k}_S$ where, $\mathbf{k}_I$ and $\mathbf{k}_S$ indicate the propagation directions of the incident and scattered light while $\mathbf{e}_I$ and $\mathbf{e}_S$ represent polarization vectors of the incident and scattered light. For our measurements we used the back-scattering configuration shown on Figure 1.3, with the incident light traveling in *b* direction with *a* polarization which is scattered in the negative direction of *b* with *a* or *c* polarization, respectively, or written in the Porto notation $z(xy)\bar{z}$ and $z(xx)\bar{z}$.

In the case when detailed specification of the scattering geometry is unneccessary, two letters indicating the directions of $\mathbf{e}_I$ and $\mathbf{e}_S$ express the experimental scattering geometry. The orientation of polarizer and analyzer is also often indicated with respect to the laboratory axes, often conventionally denoted as HV or VV or HH, meaning that $\mathbf{e}_I$ and $\mathbf{e}_S$ is either horizontal or vertical. For example, geometry indicated in Fig. 1.3 can be denoted as HV or *b(ac)b*.

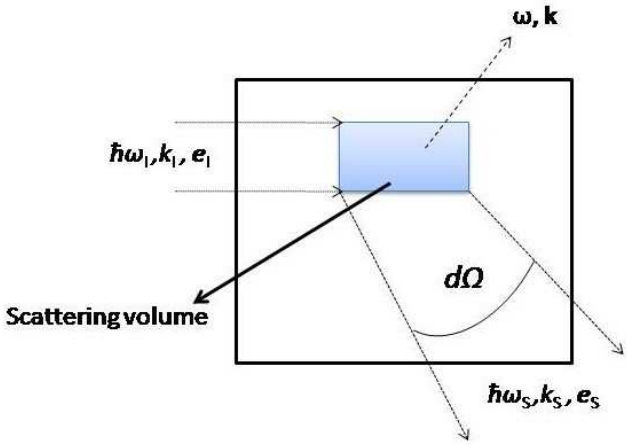

Figure 1.2 Raman scattering geometry.

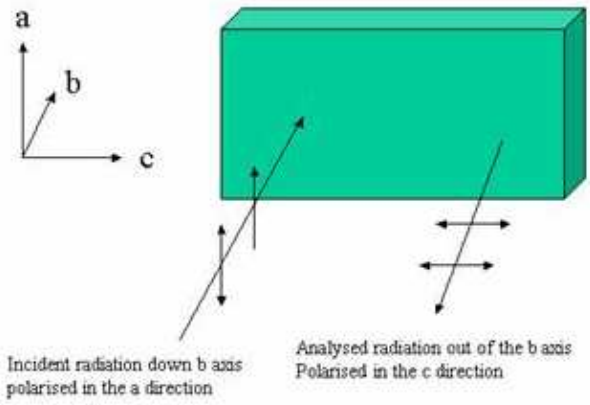

Figure 1.3 Back-scattering setup.

1.3 Experimental Techniques

1.3.1 Raman Microscopes

On many modern Raman spectrometers the integrated part of spectrometer is a microscope. The microscope has many advantages; for example, it is possible to look at extremely small samples and therefore, despite the fact that Raman scattering is weak, detect very small amounts of material. As in any optical microscopy its spatial resolution is close to the micron. Raman microscope can be also used for mapping the surface. By obtaining an accurate positional device and a suitable XYZ device one can by moving a sample and taking a Raman spectrum from small areas, map the whole sample. From this data certain vibration can be chosen and a map of the intensity variation for that vibration plotted.

A typical arrangement for the Raman microscope is shown on Figure 1.4. The more detailed description of the Raman microscope is given in [3].

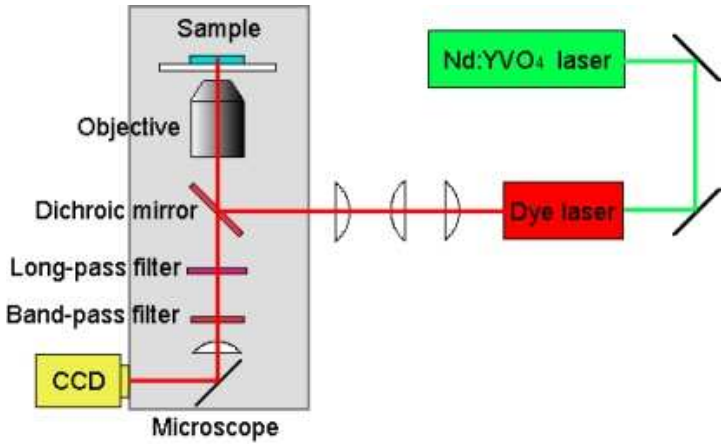

Figure 1.4 A typical micro-Raman experiment setup.

1.3.2 Experimental Instrumentation

For recording the Raman spectra in back-scattering geometry have been used a RANISHAW RM 1000 micro-Raman spectrometer shown on Figure 1.6. The instrument is characterized by dispersive operation with a single-grating monochromator, multichannel CCD detector and a simple optical path, resulting in high through output and operating convenience. For lowering the Rayleigh cut-off frequency, the holographic notch filters has been replaced with an additional monochromator (NExT filter). Two excitation sources, the 514.5 nm Ar line and the 632.8 nm He-Ne line can be used with a typical power ~ 10 mW focused through a modular LEICA DMLM microscope on a ~ 20 μm spot. The instrument configuration granted spectral resolution better than 2 cm^{-1}. A confocal setup may be used to study depth profile; a trinocular viewing head equipped with a video adapter enables microphotographs capture. The schematical layout of the RANISHAW RM 1000 microscope is drawn on Figure 1.5.

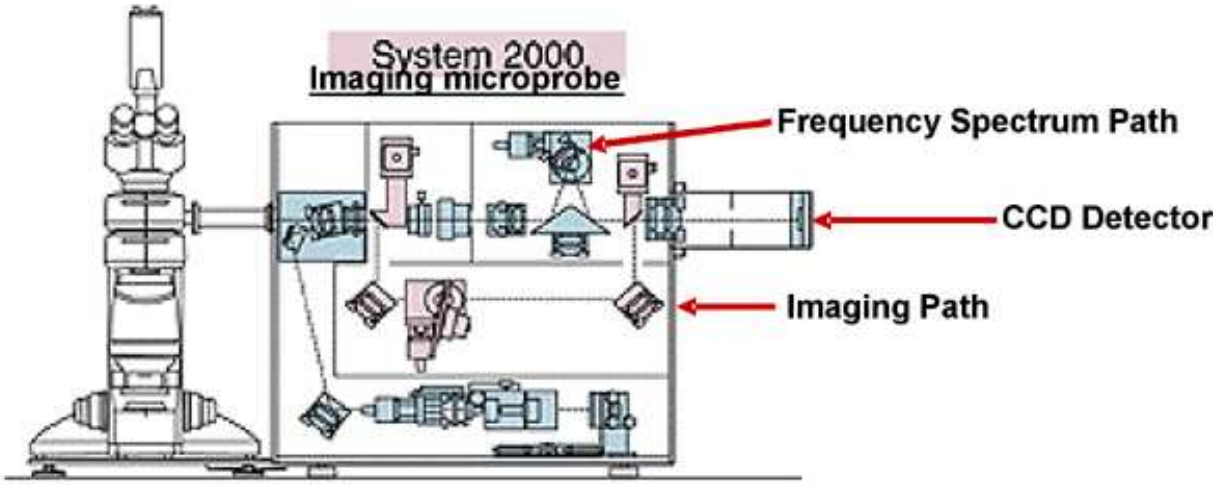

Figure 1.5 Layout of Ranishaw RM-series microscope.

Figure 1.6 Renishaw Raman microscope.

Chapter 2

The Basics of Relaxor Ferroelectrics

The relaxor ferroelectrics, or *relaxors*, exhibit many properties similar to those of spin and dipole glasses. Relaxor behavior in normal ferroelectric materials originates from compositionally induced disorder or frustration. This behavior has been most intensively studied on disordered ABO_3 perovskites and it is one of the hot topics in ferroelectrics [4, 5]. Two important characteristics of relaxor state are the existence of the dipolar nano-domains and the presence of some degree of correlations among domains. Evidence for such cooperative effect comes from the observation of some remanent polarization in electric field hysteresis loops as well as in deviation from Curie-Weiss behavior in the temperature dependence of ε'.

2.1 Relaxor versus Normal Ferroelectric

A universal property of the relaxor state is a broad frequency-dependent peak in the real part of the temperature-dependent dielectric susceptibility χ'(or $\varepsilon'=4\pi\,\chi'$). The peak defines a dynamic freezing or glass-like state transition temperature, T_m. The strong frequency dispersion in $\varepsilon'(\mathrm{T})$ on the lower-temperature side of T_m (Figure 2.2 (c)) is associated with the slowing down of dipolar fluctuations within the polar nanodomains.

In addition to a broad, frequency-dependent peak in $\varepsilon'(\mathrm{T})$ relaxors are characterized by the absence of macroscopic phase (symmetry) change at the transition. However, there is symmetry breaking at the nano-meter scale, leading to the formation of polar nanodomains (PNR's) that exist well above the peak in the susceptibility and, strongly affect the properties.

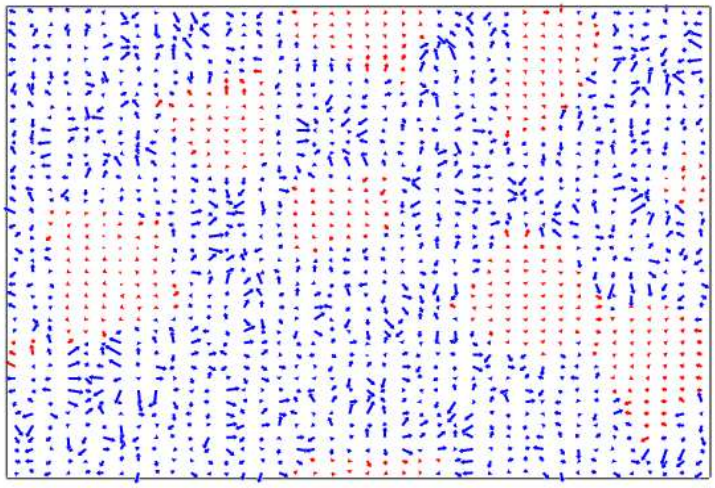

Figure 2.1 A (110) plane through the $Pb(Sc_{1/2}Nb_{1/2})O_3$ (PSN) simulation box representing the projected local field (arbitrary units) at each Pb site in the plane. Chemically ordered regions (approximately circular) have small approximately homogeneous fields, and chemically disordered regions have larger more varied and disordered local fields [6].

It is believed that the relaxor behavior is associated with the presence of chemically ordered regions or polar nanodomains (Figure 2.1). Indeed, such nanodomains have been observed in many ABO_3 relaxors at temperatures far above the peak in $\varepsilon'(T)$ [4,6]. We picture a distribution of sizes of such nanodomains in which the orientational degrees of freedom are correlated within each domain, but uncorrelated across the various domains, as shown on Figure 2.1.

For more understanding image of relaxors, it is more appropriate to compare their properties with those of normal ferroelectrics. Figure 2.2 shows the main characteristics of both relaxor and normal ferroelectrics. Description of Figure 2.2 and the differences between normal ferroelectrics and relaxors are more detailed described in Ref. 4.

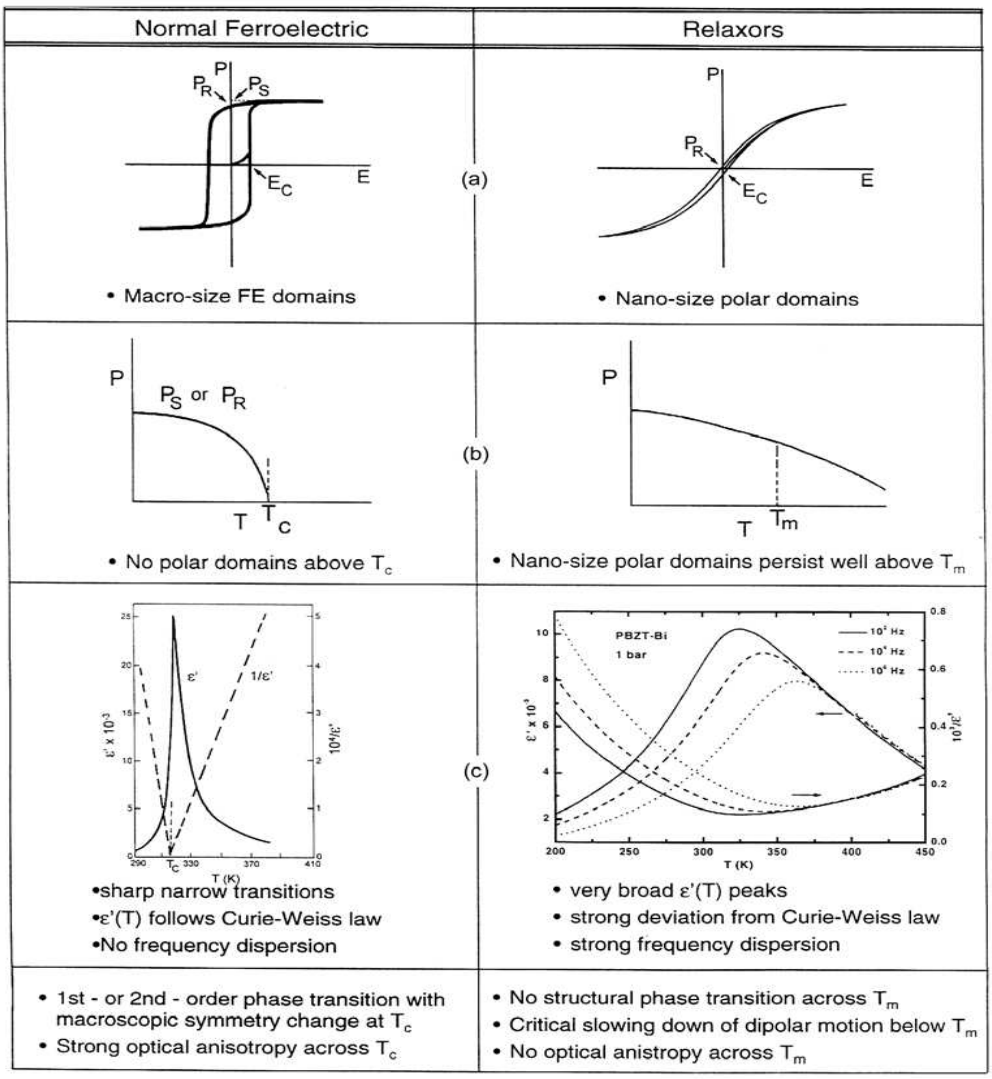

Figure 2.2 Contrast between properties of normal ferroelectrics and relaxors [4].

2.2 Lead Magnesioniobate, $Pb(Mg_{1/3}Nb_{2/3})0_3$ (PMN)

Despite the fact that is perhaps the simplest of the strong ABO_3 relaxor type, PMN remains challenging task for scientists, despite very extensive research. The disorder that is believed to be responsible for the relaxational properties of PMN is caused by differences in valence (Nb^{5+} vs. Mg^{2+}), ionic radii (0.64 vs. 0.72 Å) and electro-negativities (1.6 vs. 1.2 on the Pauling scale) between niobium and magnesium ions on the B site which produce charge fluctuations and local order. This order is the origin of the nanodomains in PMN.

Relaxor-ferroelectric solid solution of (1-x)$PbMg_{2/3}Nb_{1/3}O_3$- $x$$PbTiO_3$ are among the key object of modern physics of ferroelectrics and related materials. Doped with $PbTiO_3$ (PT), PMN exhibits a drastic increase in piezoelectric properties (increasing both the maximal value of dielectric permittivity ε and the temperature T_m of the ε (T)) [7]. Depending on the content of PT the compound has different behavior. The PMN-PT materials with low PT contents (*<30%*) posses the relaxor behavior and undergo the *rhombohedral (R3m) -> cubic (Pm3m)* structural phase transition [8]. The solutions with high PT content (*>38%*) exhibit the ferroelectric behavior and the presence of the *tetragonal (P4mm) -> cubic (Pm3m)* phase transition [9]. These two regions are separated by so called morphotropic phase boundary (MPB). The MPB (0.30 < x < 0.40) is intensively studied because the excellent electro-mechanical properties and the giant piezoeffect. At the MPB composition, the relaxor and the ferroelectric are somehow balanced, hence, the conversion between nanodomains (relaxor nature) and macrodomains (ferroelectric nature) can be better studied in the MPB systems.

2.3 Lead titanate, $PbTiO_3$ (PT)

The x=1 end-member compound of (1-x)$PbMg_{2/3}Nb_{1/3}O_3$- $x$$PbTiO_3$ and many other relaxor solid solutions is $PbTiO_3$, or PT, shown on Fig. 2.3. It is a popular model system for various phenomenological and first-principal-based calculations. It is a prototype ferroelectric perovskites crystal with a fairly high Curie temperature (T_C = 760 K) and a large spontaneous strain. In contrast to many other ABO_3 perovskites with a ferroelectric soft mode, such as $BaTiO_3$, $SrTiO_3$ or $KNbO_3$, the eigenvector of the PT soft mode corresponds primarily to A atoms vibrating against the BO_6 octahedra, i.e., to the so called Last mode, described in Ref. 5.

In materials science, lead titanate is frequently used to dilute other complex lead-based perovskites, such as $Pb(Mg_{1/3}Nb_{2/3})O_3$ or $Pb(Zn_{1/3}Nb_{2/3})O_3$ to increase their piezoelectric properties by increasing their phase transition temperature or by bringing them closer to morphotropic phase boundary (MPB) [9,10].

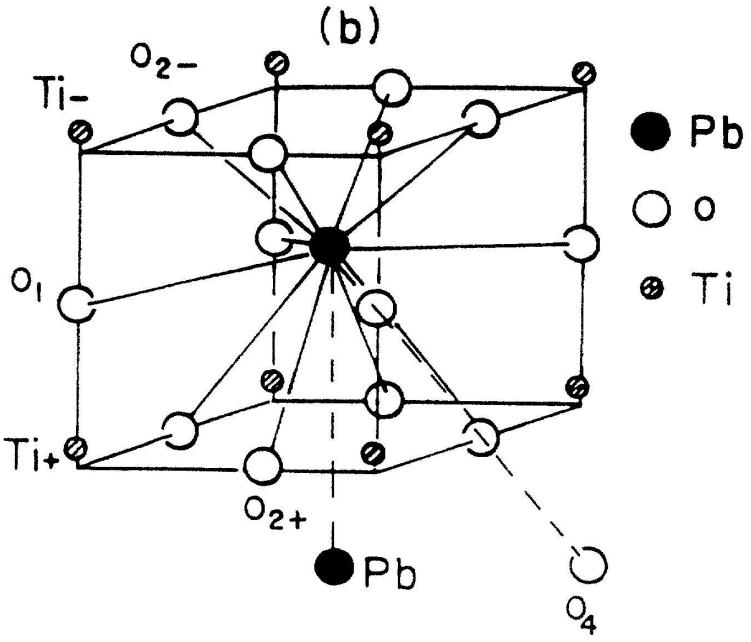

Figure 2.3 Schematical structure of $PbTiO_3$ around Pb [11].

2.4 Applications

Relaxors possess very large dielectric constants, attractive for capacitors; exceptionally large electrostrictive coefficients, important for actuators and micro-positioners; and large electro-optic constants, useful for information storage, shutters and optical modulators. Because of these remarkable properties and their applications, relaxors are one of the most active current research areas of ferroelectricity.

Relaxor-ferroelectric $PbMg_{2/3}Nb_{1/3}O_3$-$PbTiO_3$ single crystals exhibits outstanding electro-mechanical properties and are potential material for sonar applications.

Chapter 3

Measurements

3.1 Experimental Procedure

The experiments were performed on two single-crystal compounds, pure PT and PMN30%PT, with the same apparatus' configuration. Instead of the XYZ device, we used angular rotator to examine the spectra in dependence of the angle or orientation of the sample. In both cases a NeXT filter has been used, which suppress Rayleigh scattering but allows recording Raman spectra in the range of ~ 40 – 800 cm^{-1}. The laser power was focused to about 2µm spot inside of the crystal. We tried to set the center of rotation as accurate as possible, in our case accuracy lies within 1 µm diameter. The spectrometer was set to collect the reflected light from the 5-10 µm sample depth and within 10 accumulations of 5 second duration. Both experiments were carried out on room temperature.

3.2 $PbTiO_3$

The sample used in this study was a high-quality 2.7 mm thick single-crystal platelet with optically perfect natural faces, selected from a series of crystals grown by the flux method. The sample was mounted with its *c* axis ([001]) either horizontal or vertical, in order to access the transverse modes polarized parallel as well as perpendicular to the spontaneous polarization direction. More details on the sample are given in Ref. 12.

In the ferroelectric phase ($T<T_c \approx 493^oC$), PT is tetragonal with C_{4v}^1(*P4mm*) space group. At the Γ point in the Brillouin zone, it has $3A_1+4E+B_1$ optical-phonon modes, which originates from $3T_{1u}+T_{2u}$ mode of the parent cubic phase. All these modes are Raman and infrared active. In addition, long-range electrostatic forces raises frequencies of longitudinal modes (polarization parallel to **k**, LO) with respect to their transversal (TO) counterparts (polarization transverse to **k**).

Figure 3.1 shows the Raman spectra measured on PT for both HV and VV polarization setup in 3D representation in dependence on the angle.

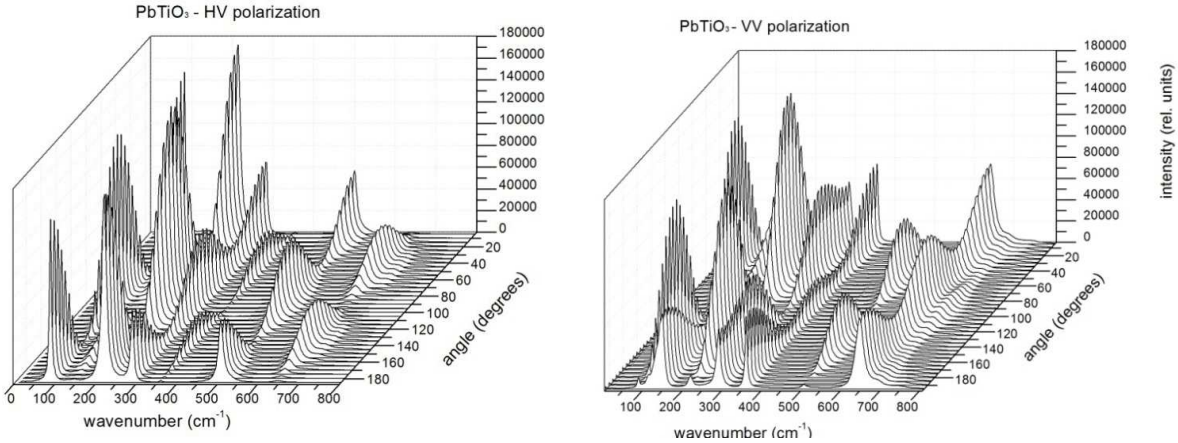

Figure 3.1 3D illustrations of the Raman spectra measured in HV and VV geometry.

Table 3.1 Frequencies (in cm^{-1}) of the principal axis TO and LO phonons at room temperature [13].

E(TO)	*E*(LO)	A_1(TO)	A_1(LO)	$B_1 + E$
87,5	128,0	148,5	194,0	289,0
218,5	440,5	359,5	465,0	
505,0	687,0	647,0	795,0	

Table 3.2 Raman tensors for tetragonal *4mm* group for the experimental setup adopted in our experiments [2].

A_1(z)	B_1	E_{TO}(y)
$\begin{pmatrix} a & \cdot & \cdot \\ \cdot & a & \cdot \\ \cdot & \cdot & b \end{pmatrix}$	$\begin{pmatrix} d & \cdot & \cdot \\ \cdot & -d & \cdot \\ \cdot & \cdot & \cdot \end{pmatrix}$	$\begin{pmatrix} \cdot & \cdot & \cdot \\ \cdot & \cdot & f \\ \cdot & f & \cdot \end{pmatrix}$

In Table 3.1 are summarized frequencies of the modes in PT measured in Ref. 13. Further on, the modes that arise from the 3 T_{1u} modes will be labeled in sequence 1, 2 and 3 from low to high frequency. So the three *E*(TO) modes will be called *E*(1TO), *E*(2TO) and *E*(3TO) (as they are arranged in columns in Table 3.1). Table 3.2 represents the Raman tensors for each mode observed in our experiments, which helps us to interpret the shape of the angular dependence of the intensity.

General equation for the behavior of intensity for VV and HV geometry is given in Eq. 3.1 and Eq. 3.2, resp., assuming a general 3x3 symmetric Raman tensor with the z axis coinciding with the axis of rotation of the sample. Vectors on the left and right side of the tensorial product corresponds to the polarization of incident and scattered light, as in Eq. 1.8.

$$\left|(\cos\varphi,\sin\varphi,0)\begin{pmatrix} a & c & \gamma \\ c & b & \beta \\ \gamma & \beta & \alpha \end{pmatrix}\begin{pmatrix} \cos\varphi \\ \sin\varphi \\ 0 \end{pmatrix}\right|^2 = \left|a+(b-a)\sin^2\varphi + c\sin 2\varphi\right|^2 \qquad (3.1)$$

$$\left|(-\sin\varphi,\cos\varphi,0)\begin{pmatrix} a & c & \gamma \\ c & b & \beta \\ \gamma & \beta & \alpha \end{pmatrix}\begin{pmatrix} \cos\varphi \\ \sin\varphi \\ 0 \end{pmatrix}\right|^2 = \left|c-2c\sin^2\varphi + (\frac{b-a}{2})\sin 2\varphi\right|^2 \qquad (3.2)$$

Depending on the symmetry of each mode, certain coefficients in the general matrix are zero. By comparing the general Raman tensor in Eq. 3.1 and 3.2 with tensors given in Table 3.2 we can claim that: for A_1 mode coefficient *c* is zero and the predicted behavior is

$$\left|\left(\frac{b-a}{2}\right)\sin 2\varphi\right|^2 \quad \text{for HV} \quad \text{and} \quad \left|a+(b-a)\sin^2\varphi\right|^2 \quad \text{for VV.} \qquad (3.3)$$

For B_1 mode the coefficients *b* and *c* are zero, so the predicted behavior should only depend on one coefficient ($a=-d$), and the predicted behavior of the B_1 mode is

$$\left|\frac{d}{2}\sin 2\varphi\right|^2 \quad \text{for HV} \quad \text{and} \quad \left|-d\cos^2\varphi\right|^2 \quad \text{for VV.} \qquad (3.4)$$

In case of the *E* mode, both the *a* and *b* coefficients are zero and the resulting function of intensity is

$$\left|f\cos 2\varphi\right|^2 \quad \text{for HV} \quad \text{and} \quad \left|f\sin 2\varphi\right|^2 \quad \text{for VV} \qquad (3.5)$$

Figure 3.2 demonstrates the behavior of intensity of the modes mentioned above, fitted with the appropriate functions. But the certain modes intensities could not be fitted with Eq. 3.3, 3.4 and 3.5 and a specific correction had to be made. First thing that is noticeable from Figure 3.2 is that the intensity changes with the 90^o rotation. That is the reason why the predicted equations (Eq. 3.3-3.5) had to be corrected by adding an appropriate trigonometric function.

The general expressions used in this case were:

$$y(\varphi)=y_0+A\sin^4(\varphi-\varphi_0)+B\sin^2(2(\varphi-\varphi_0))+C\sin(2(\varphi-\varphi_0)) \qquad (3.6)$$

$$y(\varphi)=y_0+A\sin^2(2(\varphi-\varphi_0))+B\sin^2(\varphi-\varphi_0)+C\sin(2(\varphi-\varphi_0)) + D\sin(\frac{(\varphi-\varphi_0)}{2}) \qquad (3.7)$$

For fitting we used program Origin 8 in which we can fix the certain parameter, in our case phase, and fit data globally. The advantage of global fitting is that one can represent the whole bulk of spectra measured for different angles by just a few spectra. Figure 3.3 illustrates the parameters of global fitting of the PT sample.

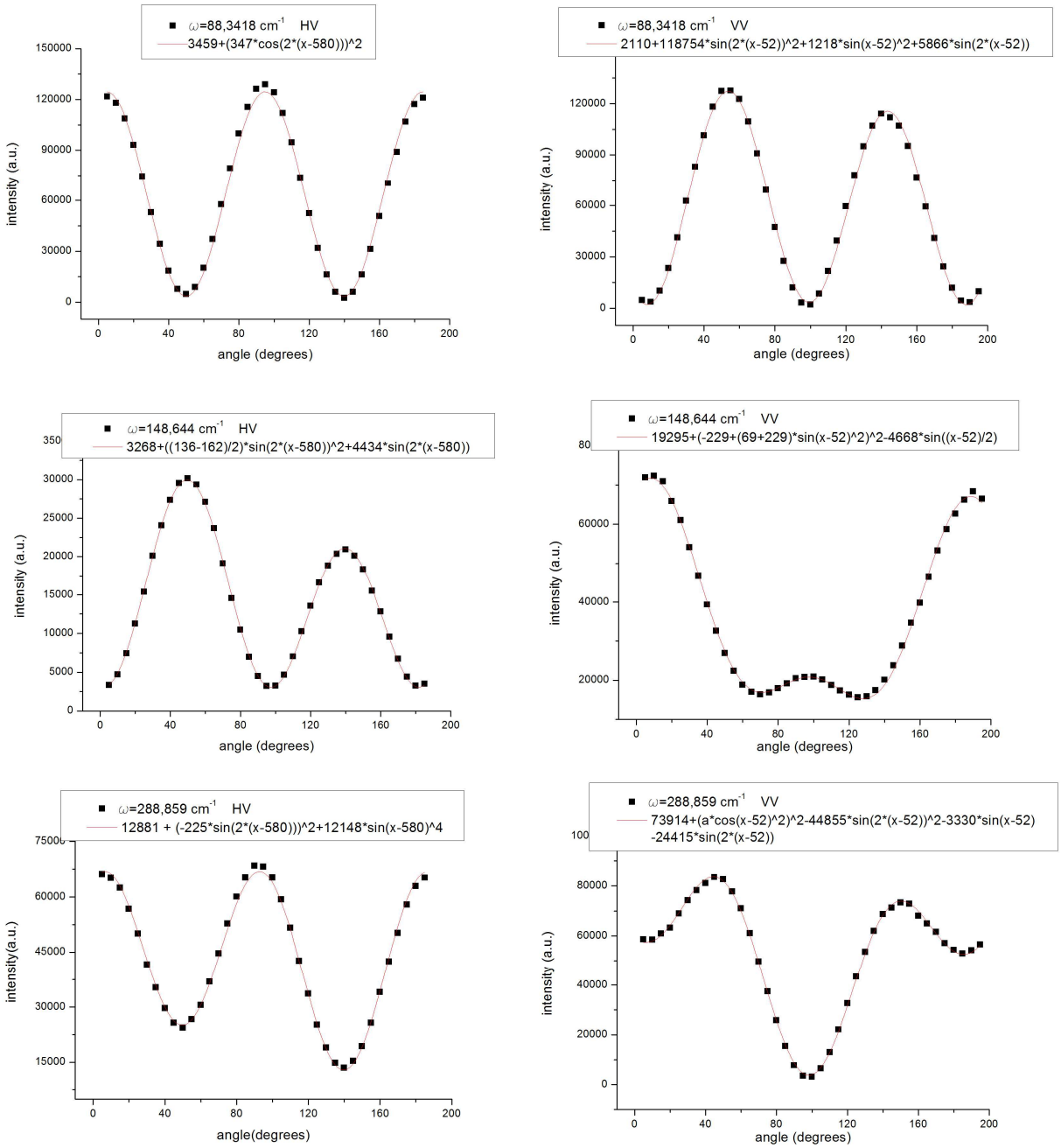

Figure 3.2 The fitted spectra of the intensity depending on the angle of orientation of the main modes of PT in *HV (graphs on left side)* and *VV (graphs on right side)* geometry.

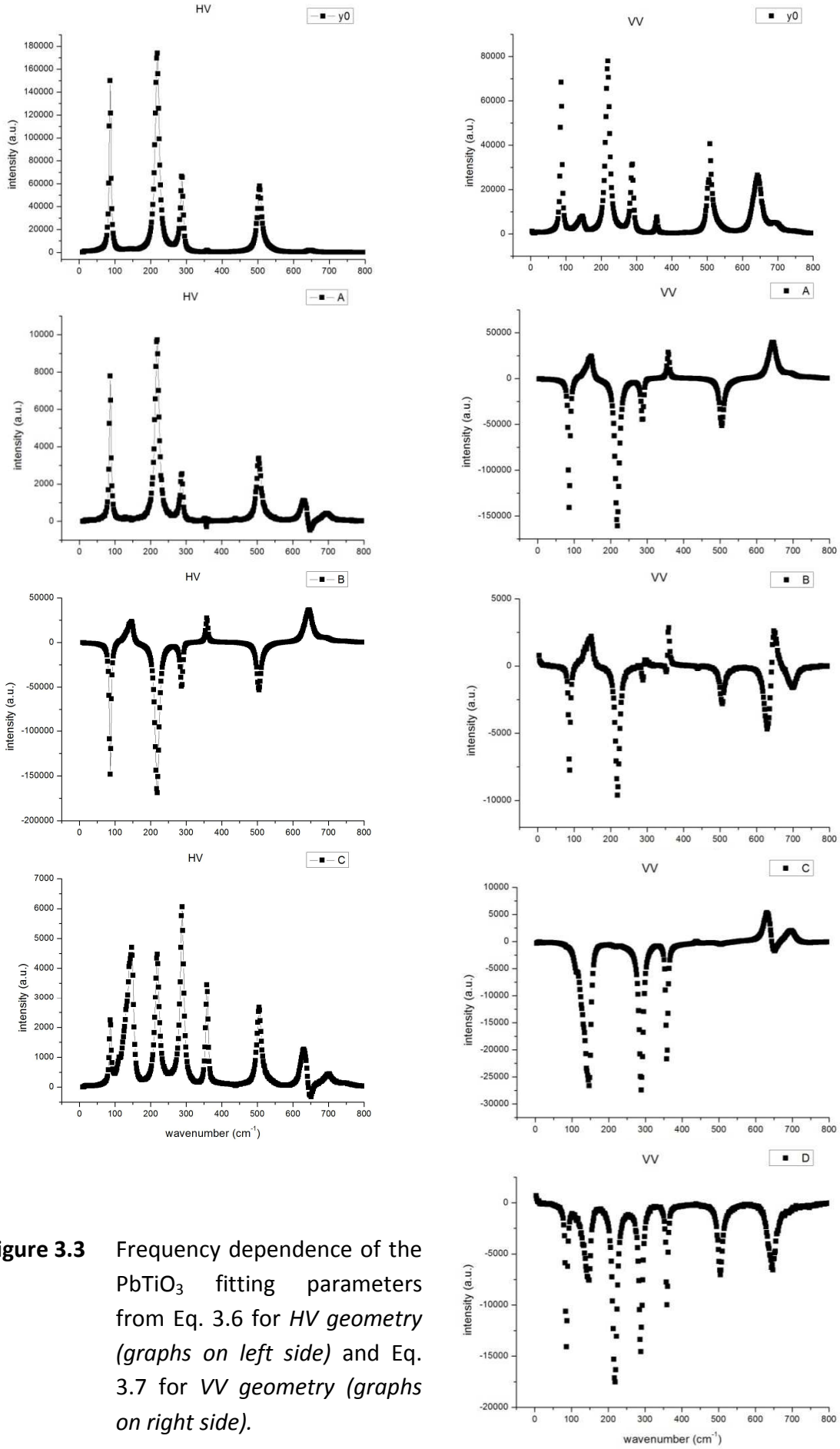

Figure 3.3 Frequency dependence of the $PbTiO_3$ fitting parameters from Eq. 3.6 for *HV geometry (graphs on left side)* and Eq. 3.7 for *VV geometry (graphs on right side).*

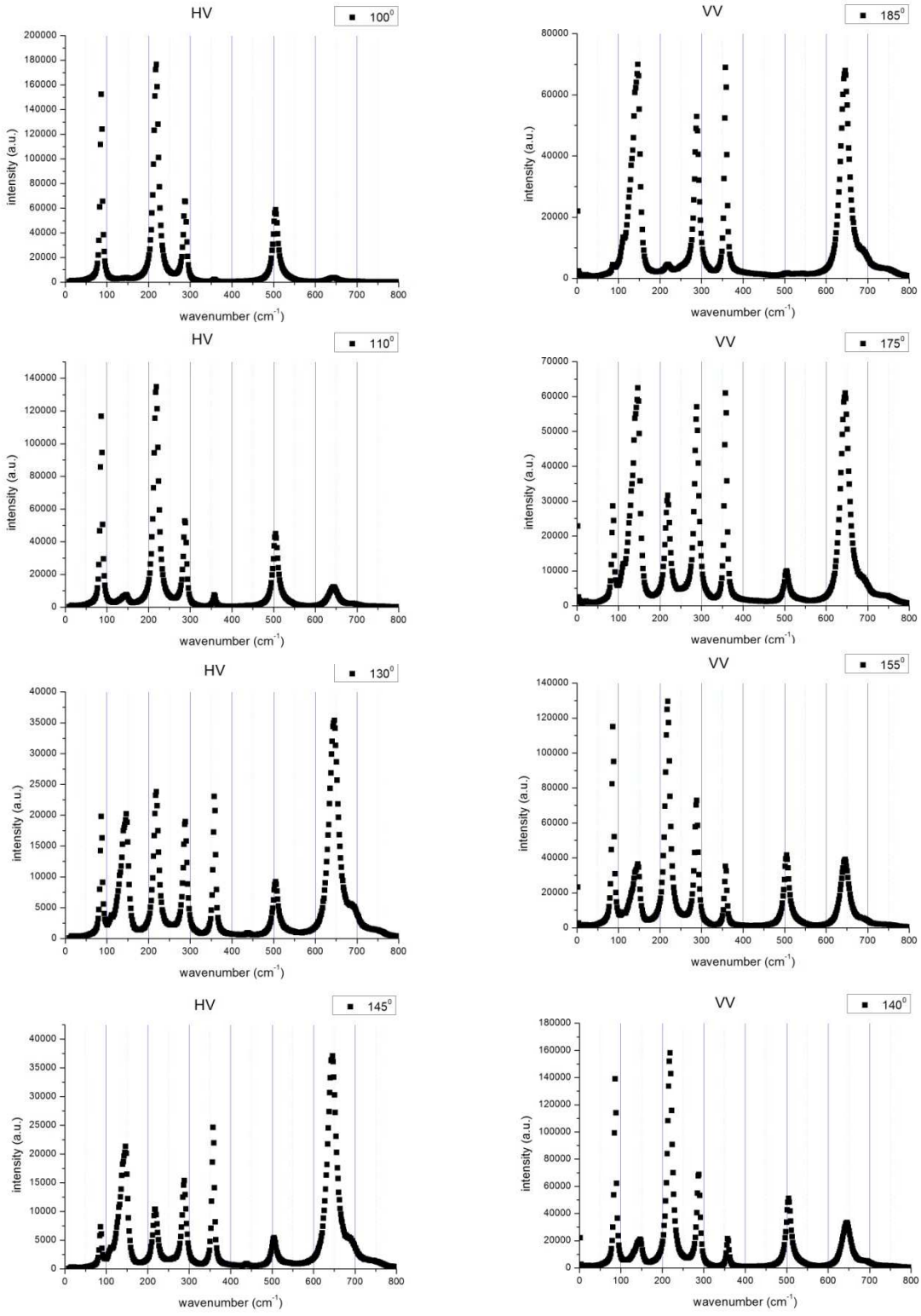

Figure 3.4 The measured spectra of PT for different angles in *HV geometry (graphs on left side)* and *VV geometry (graphs on right side)* geometry, illustrating the changes in intensity during the rotation of the sample.

Figure 3.4 is showing the change in spectrum during the rotation of the sample. The Raman selection rules for $z(xy)\bar{z}$ geometry allows here only for *E*(TO) modes and for $z(xx)\bar{z}$ geometry only A_1(TO) and B_1 ones. The top two spectra, HV for 100^0 and VV for 185^0, are similar to those published in Ref. 13, where the peak at 289 cm^{-1} is assigned to the *E*-symmetry component of the silent mode. With further rotation the spectra are changing, the A_1(TO) mode intensities are increasing in HV geometry, while *E*(TO) modes intensity increase in VV geometry. One can found the angle where only A_1(TO) and B_1 modes are recorded. This determines the direction of spontaneous polarization in the sample.

3.2.1 $PbTiO_3$ in oblique scattering geometry

For a better understanding of the differences between expected and the measured angular dependences, we measured another sample of lead titanate from the same source, but using its flat surface inclined by about 30^o from cubic crystallographic axis. In this case the asymmetry of angular dependence is even more pronounced. 3D representation of Raman spectra measured in this geometry is shown in Fig.3.5.

Figure 3.6 shows fitted spectra of the intensity depending on the angle of orientation of the main modes of this case in *HV (graphs on left side)* and *VV (graphs on right side)* geometry. For the sake of comparison, we choose the same frequencies, i.e. the same modes.

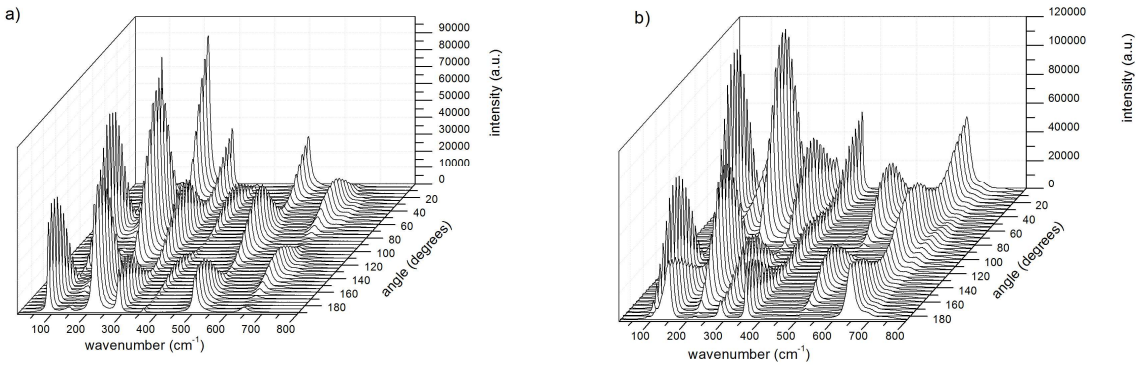

Figure 3.5 3D illustrations of the Raman spectra of PT in oblique scattering geometry measured in HV (a) and VV (b) geometry.

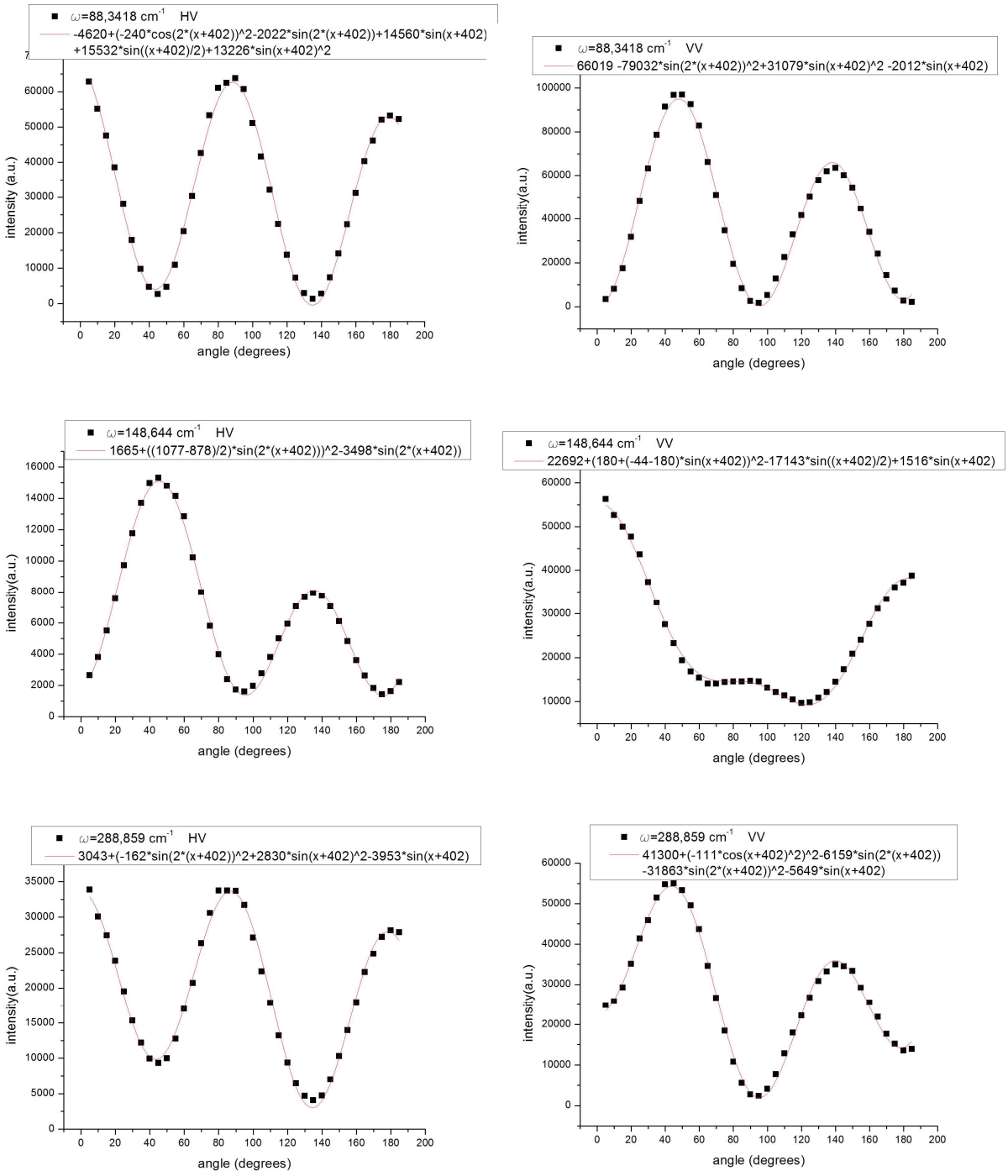

Figure 3.6 The fitted spectra of the intensity depending on the angle of orientation of the main modes of PT in oblique scattering geometry in *HV (graphs on left side)* and *VV (graphs on right side)* geometry.

3.2 70% $Pb(Mg_{1/3}Nb_{2/3})0_3$ – 30% $PbTiO_3$

The commercial example used for experiment, bought from MTI Corporation, had a light-yellow colour, a size up to 10 x 10 x 1 mm, with [001] orientation. The crystal was optically polished on one side and the sample was partly poled before using. The collection depth was set to be 10 µm.

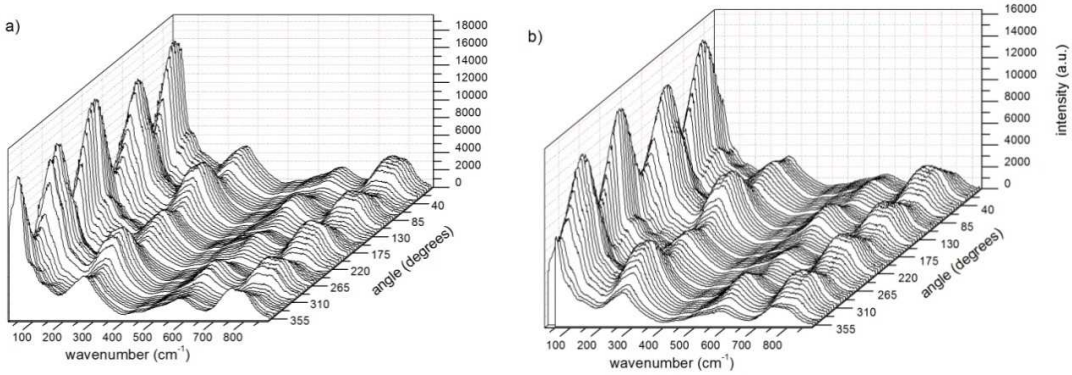

Figure 3.7 3D illustrations of the Raman spectra of PMN30%PT measured in HV (a) and VV (b) geometry.

Figure 3.7 shows the 3D representation of the Raman spectra in dependence of the angle in the HV and VV geometry. According to group theoretical analysis, 7 Raman active lines are predicted for the rhombohedral (*R3m*) symmetry:

$$\Gamma_{\text{Raman}} = 3A_1 + 4E.$$

For the tetragonal (*P4mm*) symmetry 8 Raman active lines are predicted:

$$\Gamma_{\text{Raman}} = 3A_1 + B_1 + 4E.$$

However, none of the assignment is supported by the angular dependence observed.

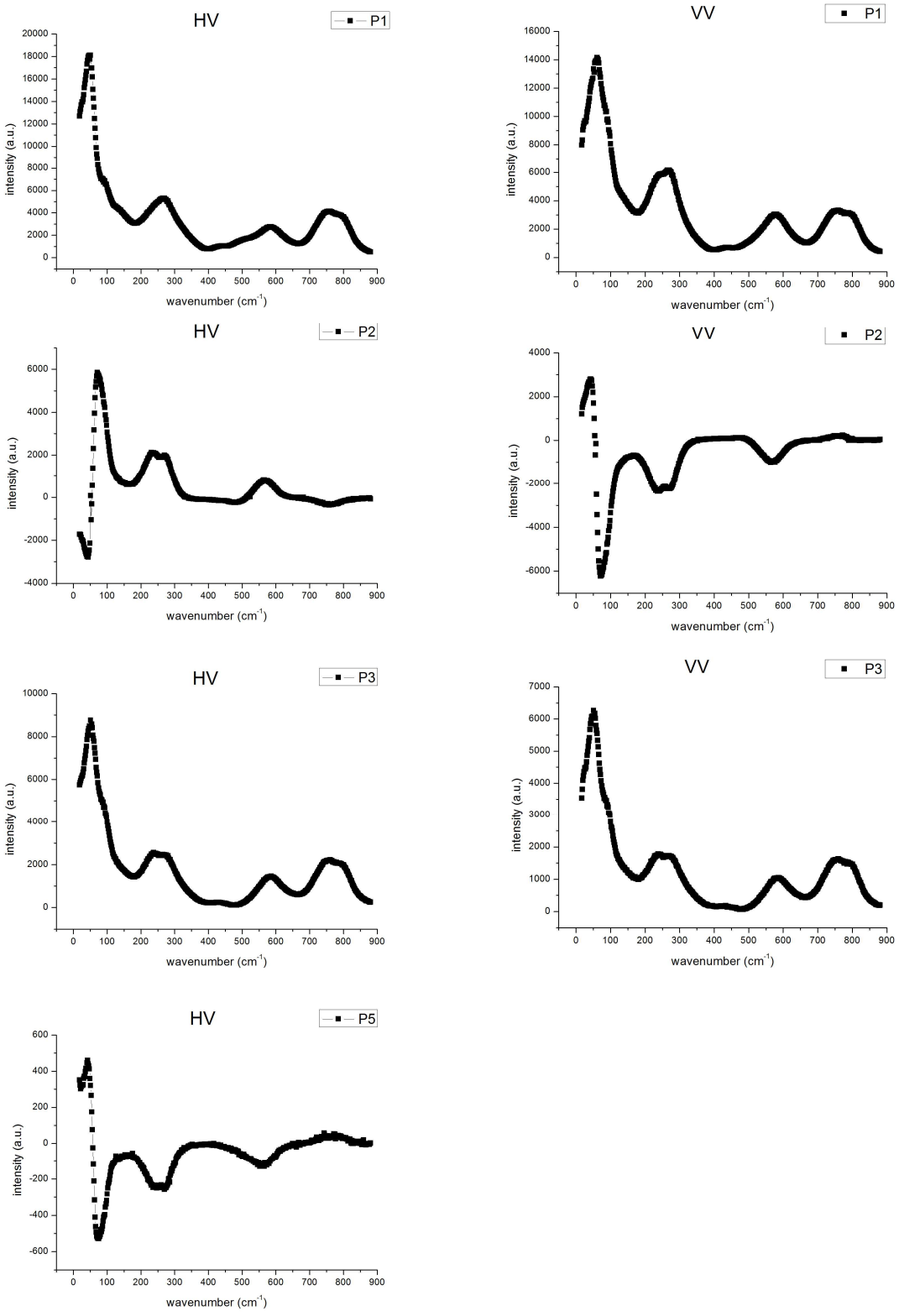

Figure 3.8 Frequency dependence of the PMN30%PT fitting parameters in *HV geometry (graphs on left side)* and *VV geometry (graphs on right side)* fitted with Eq. 3.9 (HV) and Eq.3.8 (VV).

For the VV geometry we used fitting function

$$y(\varphi) = P1 + P2\sin^2(\varphi - P4) + P3\sin^2(2(\varphi - P4)) \quad (3.8)$$

and for the HV geometry

$$y(\varphi) = P1 + P2\sin^2(\varphi - P4) + P3\sin^2(2(\varphi - P4)) + P5\sin(2(\varphi - P4)) \quad (3.9)$$

By observing Figure 3.7 one can conclude that the spectra of both HV and VV are pretty much the same except that the strength of the main mode in the HV geometry which is stronger than in the VV geometry. That affects the fitting parameters as well. This can mean that there exists a mode which contributes to the mode situated near 50 cm^{-1} which is visible in HV but not in the VV geometry. By analyzing the parameters in Figure 3.8 one can notice that the P1 parameters, expect the mode B_1 in VV and the strength of the first mode in HV, have the same shape as well as the other parameters. Table of the modes of PT is given in Ref. 13, but for PMN-PT there is no precisely given table, just a summary of the progress on PMN-PT illustrated in Ref. 7.

From our data we can resume that the spectrum of PMN30%PT consists of about 7 for HV and 8 Raman bands for the VV geometry. These bands are situated near 50 cm^{-1}, 90 cm^{-1}, 140 cm^{-1}, 240 cm^{-1}, 270 cm^{-1} (only in VV), 430 cm^{-1}, 570 cm^{-1}, 750 cm^{-1} and 800 cm^{-1}. Bands near 50 cm^{-1} and 85 cm^{-1} could be 1TO modes, which show both in pure PMN and PMN-PT at MPB, while the 2TO modes could be those situated near 230 cm^{-1} and 250 cm^{-1}. According to Ref. 13 and 7, four modes situated near 780, 570, 270 and 50 cm^{-1} correspond mainly to Nb-O-Mg stretching mode, oxygen bending vibration, B-site ion against O stretching vibration inside the octahedral and Pb against BO_6 octahedra translational vibration, respectively. Three of these, 780, 580 and 270 cm^{-1} are essentially temperature independent, while the Pb mode at 50 cm^{-1} shows strong temperature dependence. From Figure 3.7 can be seen that the main mode, situated near 50 cm^{-1} is actually consisting of two modes. The splitting of this mode near 50 cm^{-1} at low temperatures has been observed also in Ref. 13.

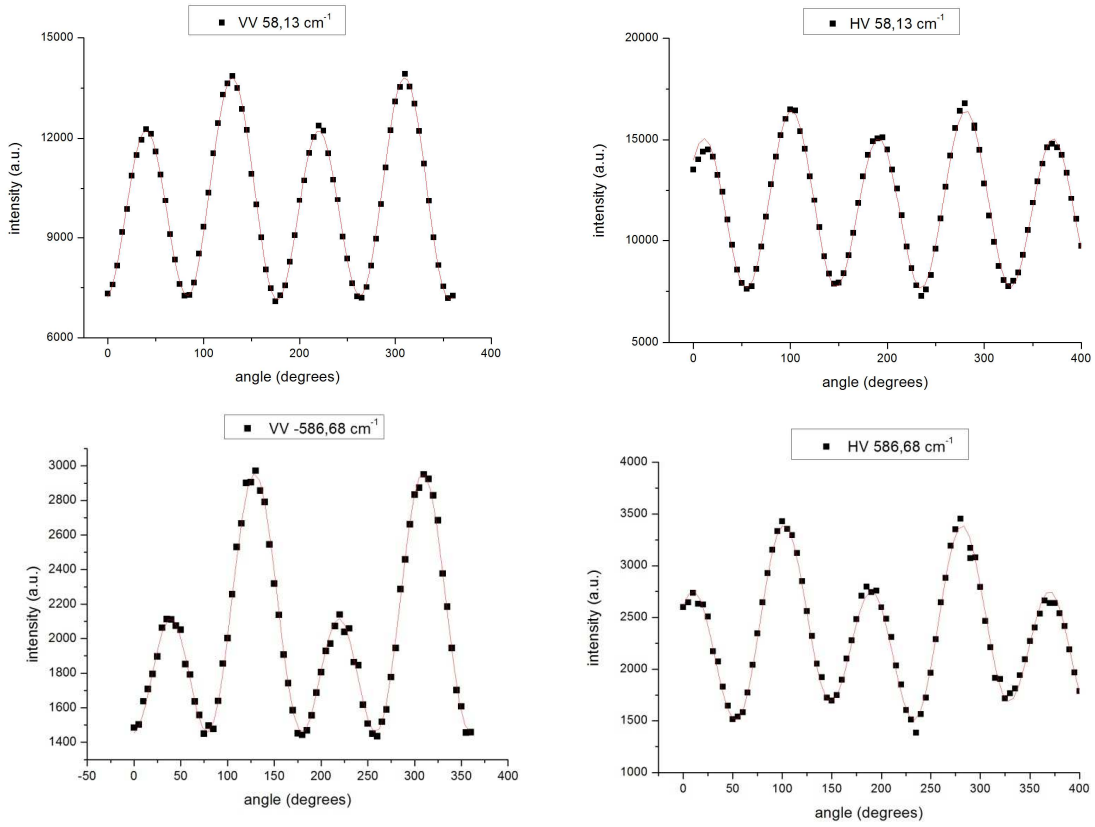

Figure 3.9 Fitted modes of PMN30%PT illustrating the deviations of the measured intensity from the expected behavior.

Chapter 4

Discussion and Conclusions

By comparing Table 3.1 with our $PbTiO_3$ data plotted on Figure 3.1 we can resume that all the modes from Table 3.1 were observed, except the A_1(LO) modes. Mode A_1(2LO) can be seen for certain angles as well as the mode A_1(1LO). Generally, the LO modes are weaker than the TO modes.

The angular dependence of the Raman intensity of $PbTiO_3$ mode mostly corresponds to theoretical expectations. Still, systematic deviations from the predicted behavior of the modes were observed. Thus, fitting curves used in Fig. 3.2 include extra asymmetric terms missing in the formulas derived from simple theoretical considerations (Eq. 3.3-3.5). Because of this, additional measurements were performed on same sample but with different setup geometry. Asymmetric deviations are even more pronounced when analogical measurements are performed in oblique incidence geometry (Fig. 3.6) discussed in part 3.3. These deviations are most probably related to finite aperture of the objective used in micro-Raman experiment. Similar effects were indeed discussed in Ref. 14.

From spectra in Figure 3.4 is noticeable that the A_1(1TO) mode, situated near 148,5 cm^{-1}, exhibits and anomalous line shape unexpected for a single phonon. We can assume that this peak consists of more peaks, but we would need to do a temperature dependence experiment to confirm that. The description of the A_1(1TO) mode and its temperature dependence is given in Ref. 13.

First thing that is noticeable in comparison PT to PMN30%PT data, i.e. Fig. 3.1 and 3.7, is that the modes of PT are much sharper. This is because the PMN30%PT is mixed crystal and the certain disorder is included. However, this gives us an advantage in processing our data because one can easily recognize the course of each mode and fit it with an appropriate function.

The angular dependence of VV and HV intensity is not as pronounced as in case of pure PT, but it certainly bears some important information about the type of the phonon modes observed. Unfortunately, the problem of asymmetric correction terms should be solved first.

In conclusion, we have studied the polarized Raman spectra of lead titanate and PMN30%PT in both HV and VV geometry by micro-Raman method in dependence of the angle of the sample rotation. Main modes of PT have been fitted with the appropriate fitting functions and compared with the theoretical expectations. We hope that the set of recorded data will be helpful for understanding of the controversial literature about Raman scattering in relaxors.

References

[1] Brüesch P, Phonons: *Theory and Experiments II* – Springer – Verlag Berlin Heidelberg 1986

[2] Gregora I: *Chapter 2.3. Raman Scattering*. In: *International Tables for Crystallography, Volume D - Physical Properties of Crystals*, (Eds. A. Authier), London, Kluwer Academic Publishers (Dordrecht, Boston, London) 2003, pp. 314-328.

[3] Smith W E and Dent G: *Modern Raman spectroscopy – A Practical Approach*, 2005

[4] Samara G A, *Jour. Phys.: Condens. Matter* **15**, R367 (2003)

[5] Hlinka J et al., *Phase Transitions* **79**, R41

[6] Tinte S, Burton B P, Cockayne E and Waghmare U V, *Phys. Rev. Lett.* **97**, 137601 (2006)

[7] Emelyanov A S, Raevskaya S I, Savenko F I, Topolov V Yu, Reavski I P, Turik A V and Kholkin A L, *Solid State Comm.* **143** 188-192 (2007)

Svitelskiy O and Toulouse J, *Phys. Rev*. B **68**, 104107 (2003)

[8] Noheda B, Cox D, Shirane G, Ye Z and Gao J, *Phys. Rev.* B **66**,054104 (2002)

[9] Slodczyk A, Barré M, Romain F, Colomban Ph and Pham-Thi M, *J. Phys: Confer. Series* **92**, 012159 (2007)

[10] Shen M, Siu G G, Xu K Z and Cao W, *Appl. Phys. Lett.* **86**, 252903 (2005)

[11] Sicron N, Ravel B, Yacoby Y, Stern E.A, Dogan F and Rehr J.J., *Phys. Rev. B* **50**, 18 (1994)

[12] Hlinka J *et al.*, *Phys. Rev. B* **73**, 140101(R) (2006)

[13] Foster C M, Li Z, Grimsditch M, Chan S –K and Lam D J, *Phys. Rev. B* **48**, 14 (1993)

[14] Bremard C, Laureyns J, Merlin J-C and Turell G, *Jour. Ram. Spect.* **18***,* 305-313 (1987)

[15] http://cs.wikipedia.org/wiki/Soubor:Image-Ramanscattering.png